

GSA Data Repository Item 2019234

Collins, B.D. and Reid, M.E., 2019, Enhanced landslide mobility by basal liquefaction: The 2014 State Route 530 (Oso), Washington, landslide: GSA Bulletin, <https://doi.org/10.1130/B35146.1>.

DATA REPOSITORY

Data Repository File DR1. Geotechnical testing, volumetric analysis, and liquefaction analysis methods (single Adobe .pdf file contained herein with four sections of text, tables, and figures)

Appendix S1: Geotechnical laboratory testing program
(includes Figures S1, S2, S3, Tables S1, S2, S3)

Appendix S2: Methodology for calculating landslide volumes
(includes Figure S4, Table S4)

Appendix S3: Methodology for coupled poroelastic model of alluvium
(includes Figure S5, Table S5)

Appendix S4: Methodology for cyclic shearing liquefaction evaluation
(includes Table S6)

Data Repository File DR2. Mapping and soil geotechnical data (Microsoft Excel .xlsx format as a separate file with five individual sheets)

Data Sheet S1: Geologic mapping data

Data Sheet S2: Sand boil and sloss pit mapping data

Data Sheet S3: Tree height mapping data

Data Sheet S4: Soil grain size distribution data

Data Sheet S5: Soil triaxial test data

APPENDIX S1. GEOTECHNICAL LABORATORY TESTING PROGRAM

We provide details of the geotechnical testing program performed on soils sampled at the Oso landslide for completeness and also as an archive for some of the ephemeral data collected during our geologic mapping campaign. Sample locations are shown in Figure S1. All testing was performed in the University of California, Berkeley geotechnical engineering laboratory with the exception of some index testing performed by a commercial laboratory (Cooper Testing Labs, Palo Alto, California).

Soil characterization testing on field samples included grain-size distribution (ASTM D422-63, 2007), Atterberg limits (ASTM D4318-10e1, 2010), specific gravity (ASTM D854-14, 2014), and USCS soil characterization (ASTM D2487-11, 2011). On undisturbed samples that could be collected with hand-pushed brass cylinders, we performed bulk and dry density (ASTM D7263-09, 2009) and water content (ASTM D2216-10, 2010) testing. Relevant associated parameters (i.e., D_{50} , C_u , and C_c for grain-size curve data, and void ratio for density and specific gravity measurements) are provided in Table S1 for debris-flow and liquefied-pool sediment deposits, and Table S2 for sand boils as well as buried and surface alluvium from the banks of the North Fork Stillaguamish River. Grain-size distribution data for the curves presented in Figure 14 are provided in Data Sheet S4 (Data Repository File DR2).

We performed geotechnical triaxial testing on North Fork Stillaguamish River alluvium samples collected from both an unburied river sand bar immediately upstream of the slide (i.e., “surface” samples, Fig. S2) and also from the alluvium buried by the overriding landslide (i.e., “buried” samples). We collected the buried alluvium from 8-m-tall cut-bank exposures along both the north and south sides of the river during field work in September 2014 (Fig. 12); these

exposures were subsequently buried by ongoing erosion of the river banks. We collected samples using hand-pushed, 6.18 cm (2.4-inch) diameter and 15.24 cm (6-inch) tall, thin-walled brass tubes that we subsequently hand-excavated from the ground (Fig. S2). We determined field density based on the mass of soil in each tube divided by the volume of the tube. In some cases, in-situ soil resistance required us to use a small hammer and end cap to further push the tubes and collect a full sample height. This likely resulted in some minor densification of the samples, but was subsequently remedied by our laboratory sample preparation method (see below).

We present data for 6 tests performed using a strain-controlled triaxial device on samples of surface alluvium collected in July 2016. These samples represent typical alluvium in the North Fork Stillaguamish River. Whereas we performed some additional tests on buried and undisturbed (tube-sampled and subsequently extruded) samples under both stress- and strain-controlled loading (primarily for obtaining generalized elastic deformation parameters for the Biot modeling – see Appendix S3), we found that sample density in some sample tubes increased significantly due to post-sampling soil transport and extrusion. For example, upon opening each sample in the laboratory, several millimeters of settlement were observed in most tubes with a thin layer of water at the sample top. Because the original (loose) density of the samples could not be achieved through the extrusion process, we chose to prepare most samples (including all results presented in Fig. 16) using the moist-tamping method (e.g., Mulilis et al., 1977). The moist-tamping method has been shown to result in relatively homogeneous samples that behave similarly (e.g., in liquefaction tests – see Mulilis et al., 1977) to other methods (i.e., wet pluviation) that might more correctly replicate the natural fabric of alluvium

deposits but which can lead to difficulties in controlling the initial sample density (e.g., Amini and Qi, 2000). The six tests presented here (see Fig. 16) were conducted on reconstituted moist-tamped samples using six layers per sample to achieve representative field density (and thus initial void ratio) conditions. For the two “All layers” tests (Fig. 16), the samples were first extruded from their field sample brass tubes, split longitudinally in half, and separated into six layers. We performed soil characterization on each layer (Fig. S3), and then subsequently moist-tamped the soil into the identical layer order of the previously extruded sample. For “Layer 2” and “Layer 3” tests, we sieved bulk samples of the identical surface alluvium as from the “All layers” samples, and prepared full-height samples representative of the grain size distribution of the individual layers from the “All layers” samples (Layer 2 or Layer 3). These samples were also prepared in six layers, but with each layer identical to all other layers within each sample.

For all tests, we aimed for relative densities (D_r) on the order of 30 to 50% (Table S3). These values were determined to be representative of the surface alluvium based on measurements on field brass-tube samples. Relative density provides a more consistent comparison for soils of varying grain size composition (e.g., such as for the Layer 2 and Layer 3 soils) compared to void ratio or dry density (Terzaghi et al., 1996). To calculate relative density, we performed maximum and minimum density tests on each test soil (All layers, Layer 2, and Layer 3) using the Japanese standard JIS A 1224:2000 (Test Method for Minimum and Maximum Densities of Sands, translated to English by Y. Hosono; JIS, 2000). Sample dry densities ranged from 1.468 to 1.600 g/cm³ with equivalent void ratios of 0.72 to 0.87 (Table S3). The void ratio of naturally deposited sands typically ranges from 0.5 to 1.0 (Cubrinovski and Ishihara, 2002); our

reconstituted samples therefore represent typical field conditions, while still achieving the target relative density range.

Following moist-tamping, we wet the prepared samples using the vacuum consolidation method (e.g., Lade, 2016) by using a small vacuum gradient (~ 15 kPa) for high consolidation stress ($p'_0 = 100$ kPa) samples or a small gravity gradient (~ 5 kPa) for low consolidation stress samples ($p'_0 = 20$ kPa). After moving a sample to the triaxial testing frame, we used the back-pressure saturation method (e.g., Lade, 2016) to achieve saturation with B-values of greater than 0.95. For the six tests presented herein, we used a strain-controlled loading platform (moving at 1.5 mm/min = 1% axial strain per minute) under undrained conditions to induce increasing vertical stresses on the sample and measured cell pressure (σ_r), pore pressure (μ), axial load (converted to stress, σ_a), and vertical soil displacement (axial strain) at a data collection rate of 5 Hz. We conducted all tests to greater than 15% axial strain to ensure that critical-state conditions were reached and post-processed all data using standard methods (e.g., Lade, 2016) with corrections made for load rod uplift, membrane stiffness, and sample cross-sectional area using a cylindrical area correction. The data presented in Fig. 16 (deviator stress $q = \sigma_a - \sigma_r$ and mean effective stress $p' = (\sigma'_a + 2\sigma'_r)/3$) are products from calculations on these data (note that effective stress, $\sigma' = \sigma - \mu$). The p' - q triaxial data for the six tests presented here are provided in Data Sheet S5 in the Data Repository.

The “All layers” tests provided sufficient information to obtain an estimate of the critical state line (CSL, Figure 16A) (e.g., Wood, 1991; Jefferies and Been, 2015). However, a clear critical state line for the Layer 3 soil could not be defined because the two tests for this soil were conducted at nearly the same void ratio. A critical state line for the Layer 2 soil could not be

obtained because both tests fully liquefied, thereby indicating that the CSL is somewhere “below” (in void ratio vs. mean effective stress space, p') the data for these tests. Finally, we note that the values of void ratio from our testing (0.72-0.87 with corresponding porosity, $n = 0.42-0.47$; Table S3) are greater, and thus more likely to contract, compared to those used by Iverson et al. (2015) (i.e., $n = 0.36-0.38$) for the Oso landslide mass in their modeling of the landslide’s mobility. This further emphasizes the role of contractive soil behavior, albeit in the underlying alluvium, in enhancing landslide mobility.

TABLE S1. SOIL CHARACTERIZATION PARAMETERS FOR DEBRIS-FLOW AND LIQUEFIED-POOL SEDIMENT DEPOSITS

Material Sample ID#	Field density (g/cm ³)	Gravi- metric water content (%)	Specific gravity (g/cm ³)	Void ratio	Grain size characteristics				Atterberg Limits LL/PI (%)	Soil classifi- cation (USCS)*
					D ₅₀ (mm)	C _u	C _c	finer (%)		
<u>Debris flow</u>										
BDC-04112014-1	N.A. [†]	78.1	N.D. [§]	N.A.	0.036	14.7	2.5	80.0	50/11	ML
BDC-04132014-1/2/3	1.908	34.8	2.755	0.90	0.110	3.9	0.6	41.3	np [#]	SM
BDC-04132014-4/5/6	1.888	26.6	2.731	0.87	0.140	57.1	0.7	22.6	21/np	SM
KS14OS-7	N.A.	N.D.	2.767	N.A.	0.104	144.2	1.6	44.3	28/7	SC-SM
KS14OS-25	2.182	15.1	2.717	0.44	0.350	25.0	2.9	17.4	17/np	SM
KS14OS-31	N.A.	N.D.	2.760	N.A.	0.168	157.5	4.1	36.7	23/4	SC-SM
KS14OS-34	1.918	22.1	2.763	0.77	0.140	153.3	3.0	40.0	23/10	SC
KS14OS-36	1.839	22.2	2.749	0.83	0.157	56.2	3.8	34.3	16/np	SM
JAC1-041014	N.A.	N.D.	2.751	N.A.	0.038	49.8	1.2	62.4	33/9	ML
JAC2-041014	N.A.	N.D.	2.762	N.A.	0.154	23.6	3.8	29.8	19/np	SM
<u>Liquefied-pool sediments</u>										
KS14OS-13	2.015	25.3	2.768	0.72	0.299	2.4	1.0	2.7	np	SP
KS14OS-43	1.904	22.9	2.774	0.79	0.503-	2.9	1.0	3.5	np	SP

*Unified Soil Classification System (USCS) soil abbreviations are: "ML" = low plasticity silt, "SM" = silty sand, "SC" = clayey sand, "SP" = poorly graded sand.

[†]N.A. = not applicable (e.g., due to bulk sample or drying prior to testing).

[§]N.D. = not determined.

[#]np = non-plastic; liquid and/or plastic limit Atterberg test not able to be performed.

TABLE S2. SOIL CHARACTERIZATION PARAMETERS FOR SAND BOILS AND ALLUVIUM

Material Sample ID#	Dry density (g/cm ³)	Specific gravity (g/cm ³)	Void ratio	Grain size characteristics				Atterberg Limits LL/PI (%)	Soil classifi- cation (USCS)*
				D ₅₀ (mm)	C _u	C _c	finer (%)		
<u>Sand boil</u>									
SB1	N.A. [†]	N.D. [§]	N.A.	0.215	4.7	0.9	13.9	np [#]	SM
SB3	N.A.	N.D.	N.A.	0.137	44.0	4.3	35.1	np	SM
KS14OS-14	N.A.	N.D.	N.A.	0.093	3.4	1.0	39.1	np	SM
KS14OS-19	N.A.	N.D.	N.A.	0.190	2.9	1.4	10.2	np	SP-SM
KS14OS-40	N.A.	N.D.	N.A.	0.470	9.0	1.9	10.3	np	SW-SM
BDC-04132014-7	N.A.	N.D.	N.A.	0.280	3.1	1.0	3.8	np	SP
BDC-09242015-1	N.A.	N.D.	N.A.	0.134	4.0	1.3	21.1	np	SM
BDC-09242015-11	N.A.	N.D.	N.A.	0.137	3.2	1.1	19.5	np	SM
<u>Alluvium – buried**</u>									
BDC-09172014-1	N.A.	2.752	N.A.	0.460	2.6	1.1	1.9	np	SP
BDC-09182014-1/2	1.537	2.779	0.81	0.170	10.2	3.3	22.8	np	SM
BDC-09182014-4/5	1.427	2.781	0.95	0.150	60.0	3.0	35.0	np	SW-SC
BDC-09182014-7/8/9	1.494	2.764	0.85	0.220	3.8	1.4	17.0	np	SP-SM
<u>Alluvium – surface**</u>									
BDC-09232015-1/3/4	1.426	N.D.	0.94 ^{††}	0.436	3.8	1.3	4.0	np	SP
BDC-09232015-5/8	1.383	N.D.	1.00 ^{††}	0.430	2.9	1.3	4.4	np	SP
BDC-07122016-1/2/19	1.502	2.751	0.83	0.842	9.3	1.2	5.9	np	SW
BDC-07122016-7/8/20	1.524	2.776	0.82	0.529	4.8	1.0	6.3	np	SP

*Unified Soil Classification System (USCS) soil abbreviations are: “SM” = silty sand, “SC” = clayey sand, “SP” = poorly graded sand, “SW” = well graded sand.

[†]N.A. = not applicable (e.g., due to bulk sample or drying prior to testing).

[§]N.D. = not determined.

[#]n_p = non-plastic; liquid and/or plastic limit Atterberg test not able to be performed.

^{**} Although the average dry density of the buried alluvium (1.486 g/cm³; Fig. 12) is greater than the surface alluvium (1.459 g/cm³) and suggests densification by the overriding landslide, the difference is not statistically significant (i.e., the data fails a two sample t-Test) due, in part, to the small number of samples (n_{buried} = 3 and n_{surface} = 4).

^{††}Void ratio based on specific gravity from other tests of similar samples.

TABLE S3. GEOTECHNICAL TRIAXIAL TEST
 SAMPLE PREPARATION DATA FOR NORTH
 FORK STILLAGUAMISH RIVER ALLUVIUM

Confining stress (kPa)	Relative density* (%)	Void ratio
<u>All layers soil</u>		
20	30	0.83
100	36	0.81
<u>Layer 2 soil</u>		
20	45	0.72
100	42	0.73
<u>Layer 3 soil</u>		
20	37	0.87
100	41	0.86
*Relative density was determined based on maximum and minimum void ratios computed for each soil.		

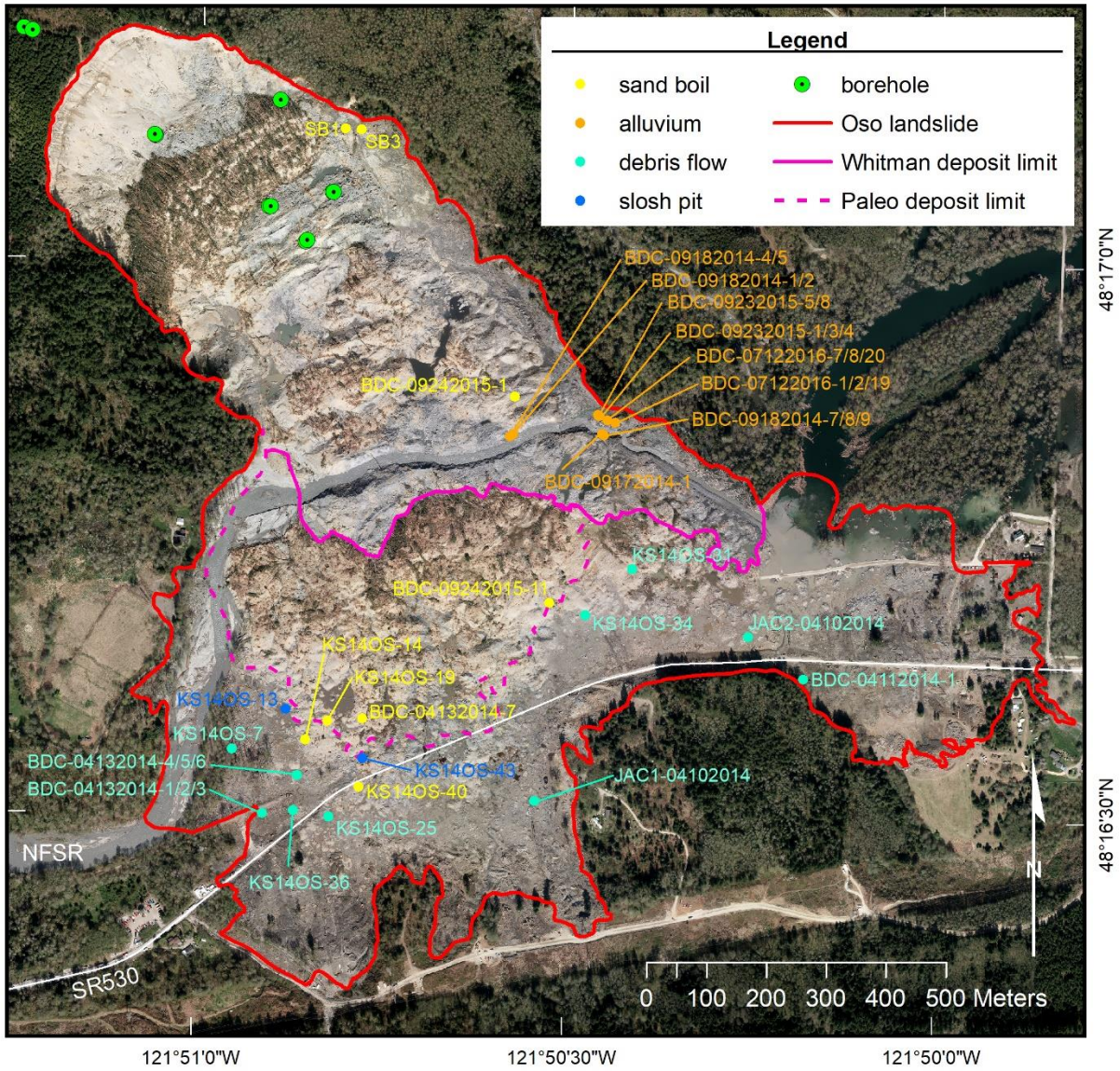


Figure S1. Map showing location of samples used in geotechnical characterization and triaxial testing. Colors denote type of sediment sample. NFSR—North Fork Stillaguamish River.



Figure S2. Soil-sampling method used to collect surface alluvium samples for geotechnical triaxial testing. The sample location is a newly formed river sand bar on the upstream end of the 2014 Oso landslide and thus representative of the surficial alluvium present in the floodplain prior to being overridden by the landslide.

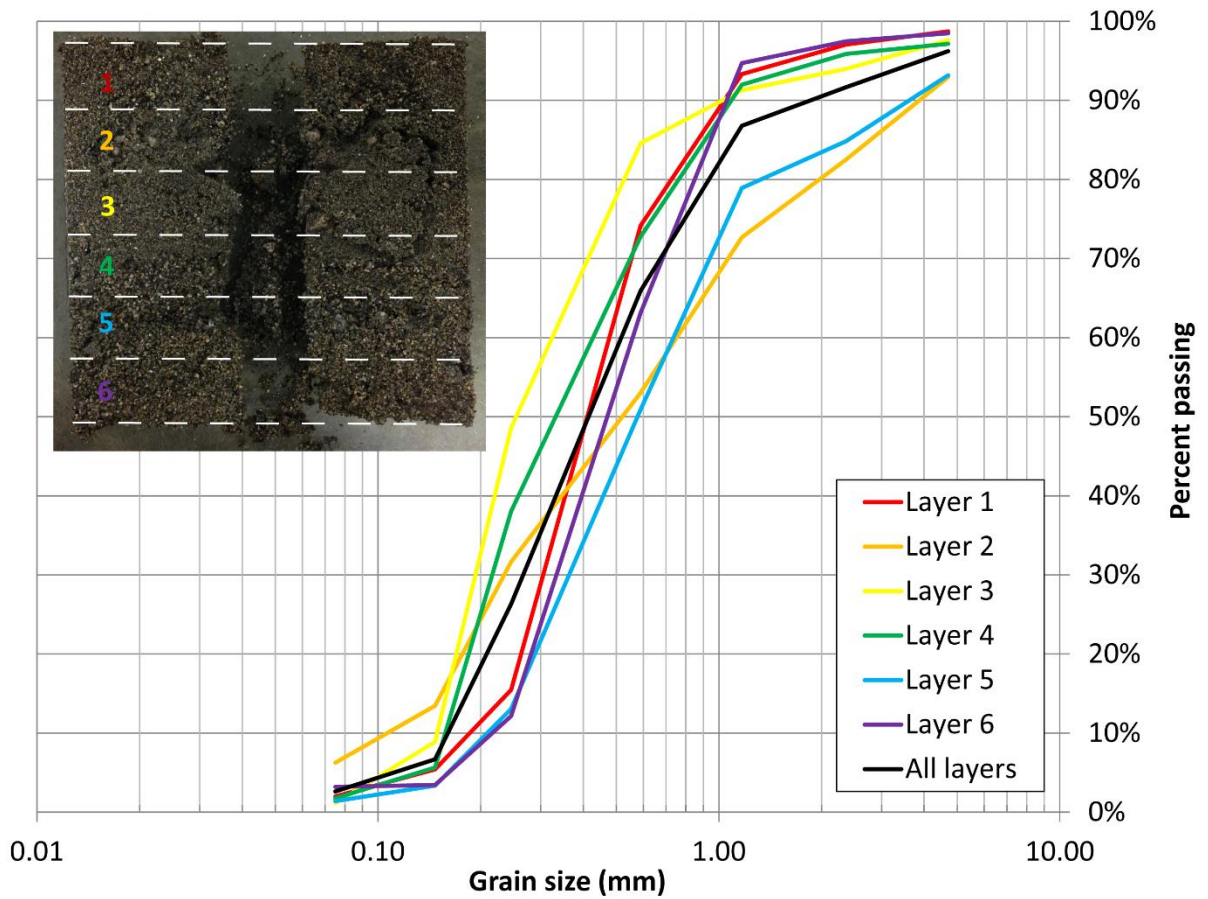


Figure S3. Soil grain-size distribution curves of individual soil layers of the alluvial sediment used for geotechnical triaxial testing to investigate the susceptibility to liquefaction failure of alluvium present in the North Fork Stillaguamish River valley bottom. Sediment layers are divided evenly but account for stratigraphic divisions observed in the soil texture. Soil layers used for triaxial testing are shown as “Layer 2”, “Layer 3”, and “All layers”.

APPENDIX S2. METHODOLOGY FOR CALCULATING LANDSLIDE VOLUMES

Our calculation of landslide source and deposit volumes relied on the construction of high resolution ground and failure surfaces using available lidar data (preslide July 2013 data available from the Puget Sound Lidar Consortium, <http://pugetsoundlidar.ess.washington.edu/> and postslide, 26 March 2014 and 6 April 2014 data provided by WSDOT, <http://www.wsdot.wa.gov/mapsdata/Photogrammetry/3DTL.htm>). Whereas ground surfaces were relatively straightforward to construct, defining the topography of the failure surfaces at depth required incorporating several sources of disparate subsurface information. These included: (1) lidar points of the exposed head and lateral scarps, (2) failure surface borehole intersections, (3) a curvilinear cross-section line connecting the boreholes to the headscarp, (4) field mapping evidence of areas outcropping near the failure surface, and (5) the mapped, three-dimensional boundary of the landslide mass.

The geotechnical drilling investigation conducted following the landslide (Badger, 2016) revealed a failure-surface depth that emplaced outwash and presumed headscarp colluvium infilling (Q_c ; Fig. 4, Fig. 8) unconformably over deeper glaciolacustrine silt and clay (Q_{glv}) just below the Whitman headscarp at an elevation of 122-124 m (WSDOT borehole EB-04si-15; Fig. 8), and approximately 80 m below the (preslide) conformable Q_{gov} - Q_{glv} contact. Further confirmation of the failure surface beneath the Whitman mass was provided by field observations where an internal slice of the Whitman component exposed a flat area (Fan Lake, Fig. 3) that, based on geometrical inferences connecting the WSDOT boreholes and the overriding surface exposed at the new alignment of the North Fork Stillaguamish River (see Fig. 12), is located close to the failure surface. An additional borehole on the upper east side of the

Whitman component (WSDOT borehole – EB-05si-15) also identifies the Whitman failure surface with displaced advance outwash (Q_{gov}) overlying glaciolacustrine deposits (Q_{glv}) at 135 m elevation, which is approximately 50 m below the expected (pre-landslide) conformable contact in that location. Note that borehole EB-05si-15 is 200 m off-section in Fig. 8 (see also Fig. 4) and therefore the stratigraphy does not match precisely the elevations shown in the section. We also used several other boreholes (H-15vwp-15, EB-07si-15, and EB-09si-15) in the failure surface construction that provide evidence of the basal shear plane.

Using this borehole information, along with the other topographic information, we created a failure surface underlying the source area and thereby calculated an estimate (lower bound) for the source area volume ($7,934,000 \text{ m}^3$). We then created a slightly more complex 3D failure surface geometry by assuming that the off-axis boreholes on the east scarp (WSDOT boreholes EB-05si-15 and EB07si-15; Fig. 4) could be mirrored and translated to similar locations along the western scarp. Similarly, we translated the curvilinear longitudinal axis cross-section line of the failure surface both to the east and west to further refine the geometry. Construction of this failure surface enabled an additional (upper bound) volume estimate of the Oso landslide source ($10,079,000 \text{ m}^3$). We report the average of these two estimates for the final estimated volume of the landslide source area (Table 1).

We similarly calculated the presumed source volumes for the two other components (Hazel slide and Paleo slide) through reconstruction and projection of visible pre-Oso landslide scarps to the depth of the reconstructed Oso landslide failure surface. For the Paleo source volume, we constructed several possible failure surfaces that intersected the existing pre-2014 geometry of the Paleo bench and identified the most plausible surface based on the measured

deposit volumes. We found that any Paleo source failure surface steeper than we present (Fig. 8) resulted in an unreasonably low (i.e., near or below zero) volumetric expansion ratio between source and deposit. Similarly, we found that any failure surface that did not include some part of the Paleo source resulted in an unreasonably large (i.e., on the order of 50%) expansion ratio. Thus, our Hazel-Paleo source failure surface is constrained by these calculations and analyses.

We determined the volumes of all components of the 2014 landslide (Whitman, Paleo, Hazel, and debris flow) by direct comparison of the triangulated irregular networks (TINs) of the constructed surfaces. For source volumes, we compared the preslide surface to the failure surface, and for deposit volumes, we compared the postslide surface to the preslide surface. Most volumes were calculated as described in the “Methods” section. To determine the volume of the debris-flow part of the landslide deposit, we measured the area covered by debris-flow veneer and multiplied this by the average flow depth measured on the back sides of still-standing trees in the distal debris field. Here we assume that the average flow depth is representative of the debris-flow deposit thickness. Flow depth measurements on standing trees were made in the weeks and months following the landslide (Fig. 11A) and consisted of three observations: the front-side scour height, the front-side (maximum) splash height, and the back-side flow depth (Table S4, Fig. S4). In most cases, measurements were made manually using a measuring tape and data were recorded to the nearest decimeter. In a few cases (splash heights greater than 3 m), measurements were estimated by referencing a measuring tape located at the lower section of the tree. Although the front-side scour and splash heights were always greater than the back-side flow depth, dynamic runup and idiosyncrasies in the

mechanics of flow (e.g., scour heights from dislodged tree limbs dragging onto in-place trees) precluded using these (front-side) measurements to estimate flow depth. Thus, the back-side flow depth provided the most realistic estimate of overall debris flow thickness at the far distal ends of the deposit. We calculated separate average flow depths in the west and east lobes based on six and seven back-side flow depth tree measurements, respectively (Table S4, Fig. S4).

To calculate the volume of water in the North Fork Stillaguamish River presumably entrained during the initial motion of the landslide across the valley, we computed a river entrainment area of 97,000 m² from widths of the river and landslide, and an average river depth of 0.8 m based on stream gage data comparison between the Arlington gage (#12167000), located approximately 23 km downstream of the landslide which was operating at the time of the landslide, and the C-Post Road Bridge gage (#12166185), located just upstream of the landslide which was installed shortly after the landslide (Magirl et al., 2015 and on-line data available from <https://waterdata.usgs.gov/wa/nwis/sw>). For this analysis, we correlated the river depth at the time of landsliding (when only the Arlington gage was operating) to the ratio of the river depth at other times of year for which both gages were in operation. For volume total calculations, we assume that the resultant volume of entrained North Fork Stillaguamish River water (78,000 m³) was integrated into the impacting slide materials (i.e., Hazel landslide source). Although there was some water visible in standing pools at the distal end of the 2014 landslide deposit immediately after the event, we believe the majority of water was incorporated into the debris-flow deposit and is therefore captured by this volume.

Given the high quality and resolution of the lidar data sets (our bare earth models of ground surfaces were each composed of approximately 2 million points with a 2-meter point spacing), we have high confidence (<1% error) in the volumes calculated for the landslide deposit areas with the exception of the debris-flow and the Whitman component. For the debris-flow volume, our estimate may be between one half to twice as large as the actual deposit volume, but cannot be constrained any further due to the difficulty in distinguishing the component of debris-flow veneer (especially reflected backwash) from the underlying Hazel component deposit. The assumptions made for the construction of the three-dimensional failure surface beneath the Whitman source area result in somewhat larger error (± 12 to 16%) for the Whitman source and deposit volumes, respectively. Overall, our volume calculations resulted in a 6% difference (i.e., landslide volume expansion ratio) between total source to deposit volume (Table 1) which appears reasonable given that the majority of interparticle motion was confined to the shear plane and that the lidar data was of sufficiently high resolution to account for most extensional voids between hummocks.

TABLE S4. DEBRIS FLOW DEPTH MEASUREMENTS FROM TREE ON-LAP OBSERVATIONS

Observation #	Easting* (m)	Northing* (m)	Flowline distance [†] (m)	Front side scour height (m)	Front side splash height (m)	Back side flow depth (m)
<u>West lobe</u>						
1	585391	5347777	303	2.5	3.8	N.D. [§]
2	585396	5347760	319	2.5	3.3	1.0
3	585386	5347754	323	1.4	2.2	0.6
4	585390	5347754	323	1.6	2.6	0.9
5	585379	5347680	386	N.D.	0.5	N.D.
6	585388	5347671	397	N.D.	1.5	N.D.
7	585384	5347669	399	N.D.	1.5	N.D.
8	585376	5347646	416	N.D.	0.5	N.D.
9	585385	5347649	417	0.6	2.0	1.2
10	585387	5347614	450	N.D.	0.8	0.6
11	585384	5347599	463	N.D.		0.5
<u>East Lobe</u>						
1	586458	5347824	850	N.D.	5.5	2.7
2	586548	5347825	892	N.D.	4.6	0.6
3	586599	5347822	921	N.D.	0.9	0.6
4	586649	5347825	942	N.D.	2.0	1.0
5	586598	5347795	944	N.D.	3.0	1.8
6	586658	5347799	971	N.D.	1.0	N.D.
7	586536	5347704	993	2.0	3.0	1.5
8	586561	5347696	1012	N.D.	1.8	0.5

*Referenced to NAD83 datum and UTM Zone 10 projection.

[†]Flowline distance is measured from the black dashed line in Fig. 6 along flow paths that mimic the slight spread of the deposit (i.e., “0” distance indicates the northern limit of alluvium as defined in 2003 aerial imagery – see also Fig. 3).

[§]N.D. = No data indicates field measurement was not possible or was not clearly visible.

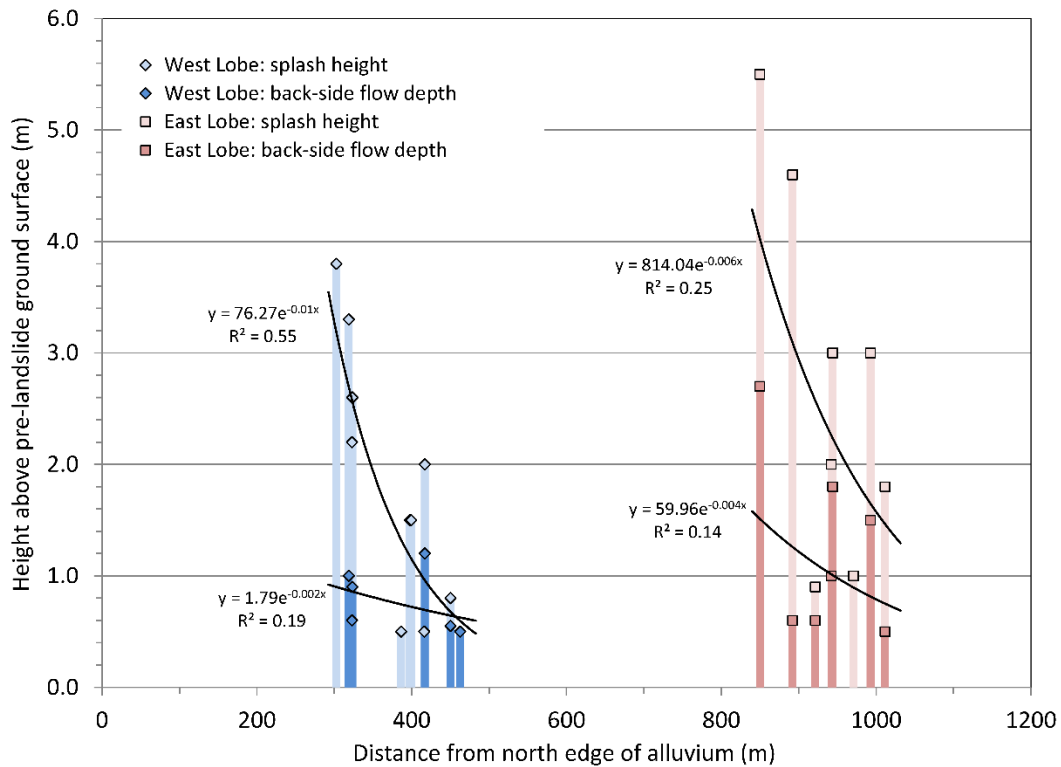


Figure S4. Transient debris-flow back-side flow depths and front-side splash heights in the distal lobes based on field measurements of mud-lines on still-standing tree trunks at the edges of the deposit. Distances are measured from the approximate north edge of valley alluvium (see Fig. 6) along inferred flow lines that mimic the slight spread of the deposit to the west and east. A rough exponential decline is fit to the data, and overall flow depths averaged 0.8 m and 1.2 m respectively for the west and east lobes of the deposit. Maximum splash heights of 3 to 6 m above the ground surface attest to the rapid and surging nature of the debris flow even as it flowed to the far side of the valley.

APPENDIX S3. METHODOLOGY FOR COUPLED POROELASTIC MODEL OF ALLUVIUM

To assess potential pore-water pressure increases from rapid loading, we used a two-dimensional, finite-element poroelastic numerical code (Biot2) that couples groundwater flow with elastic deformation in a fluid-filled porous medium. This approach is based on Biot theory and assumes isothermal deformation governed by linear elasticity and Darcian fluid flow with uniform density and viscosity (Biot, 1941; Rice and Cleary, 1976; Hsieh, 1996); displacement, strain, stress, and pore-water pressure or hydraulic head are calculated over time. For our simulations, the dynamic interactions between pore-water pressure and deformation are controlled by the parameters listed in Table S5. We estimated the parameters for the North Fork Stillaguamish River alluvium using results from our drained and undrained triaxial tests (see Appendix S1). In these tests, we used extruded, intact alluvium samples as well as stratified and homogenized samples under both stress and strain-controlled loading. For our model simulations, we used typical drained values.

To simulate loading by an overriding slide mass, we assumed a vertical domain representing a cross-section through 10 m of alluvium (Fig. S5); we also assumed plane strain in the third dimension. We divided the domain into 10 cm square elements as this resolution allowed reasonable simulations of dynamic response during loading given the parameters in Table S5. Boundary conditions for displacement permitted vertical (but no horizontal) displacement on the lateral margins, lateral (but no vertical) displacement on the bottom, and no traction on the ground surface prior to loading. Groundwater flow boundaries allowed no flow on the lateral and bottom boundaries, with a constant zero pressure head at the ground surface. Initial pore-water pressures, prior to loading, mimicked fully saturated, hydrostatic conditions.

We simulated dynamic transit of a moving landslide across the domain by applying a known vertical traction to the top face of each ground-surface element in sequence from the left boundary to the right (i.e., simulating landslide loading from north to south). The propagation of the loading front replicated a landslide speed of 10 m/s (estimated from a runout distance of approximately 1000 m for the majority of the landslide materials over a period of 100 seconds (Iverson et al., 2015)). In a single simulation, each 10-cm ground-surface element was sequentially loaded by 100 kPa (equivalent to the vertical loading from about 5 m of saturated slide material with a unit weight of 20 kN/m³) over 0.01 s. During this short time, the load at that element increased linearly from zero to the maximum (100 kPa), then remained at the full load as the simulated front moved forward to the next element. The simulations did not include transient impact loading or boundary stresses modified by slide velocity. Dynamic loading caused the sediment to deform and pore-water pressures to increase from hydrostatic. Pore pressures could dissipate upward from the unloaded ground surface immediately in front of the simulated overriding slide mass; however, they were not permitted to dissipate into the overriding mass, as this was assumed to be much less permeable than the alluvium.

We performed sensitivity tests to examine the relative importance of different sediment parameters. All parameters could modify simulated pore-pressure responses, but values of shear modulus and hydraulic conductivity exerted stronger influences. Nevertheless, the overall patterns of pore-pressure response were similar given reasonable variations in parameters (Table S5). Modifying the thickness of alluvium to 5 m also did not greatly change the responses. The amount of vertical traction applied (i.e., loading from increased overriding

landslide thickness) did have a profound influence on pore-pressure responses, with pressures increasing in an approximately linear manner to the applied load.

TABLE S5. ALLUVIUM PARAMETERS USED IN BIOT MODELING

Parameter*	Units	Laboratory test values			# of meas.	Biot model value
		Average	Maximum	Minimum		
Porosity	N.A. [†]	0.457	0.467	0.445	7	0.46
Drained Poisson ratio [§]	N.A.	0.37	0.5	0.12	3	0.37
Drained elastic modulus [§]	N/m ²	2.12×10 ⁷	3.00×10 ⁷	1.60×10 ⁷	3	2.1×10 ⁷
Drained shear modulus [#]	N/m ²	7.74×10 ⁶	1.09×10 ⁷	5.84×10 ⁶	3	7.7×10 ⁶
Saturated hydraulic conductivity	m/s	4.75×10 ⁻⁵	7.00×10 ⁻⁵	2.46×10 ⁻⁵	4	4.8×10 ⁻⁵
Specific weight of water	N/m ³	N.A.	N.A.	N.A.	N.A.	9.8×10 ³
Bulk modulus of water	N/m ²	N.A.	N.A.	N.A.	N.A.	2.2×10 ⁹
Alluvium thickness ^{**}	m	4.1	13.4	0.6	12	10

*Porosity, stiffness parameters, and hydraulic conductivity measured from laboratory tests conducted as part of this investigation.

[†]N.A. = not applicable.

[§]Determined at 0.5% strain.

[#]Calculated from elastic modulus assuming Poisson ratio of 0.37.

^{**}Thickness estimated from SR530 reconstruction boring logs (Fiske, 2014). The alluvium may be thicker closer to the slide origin.

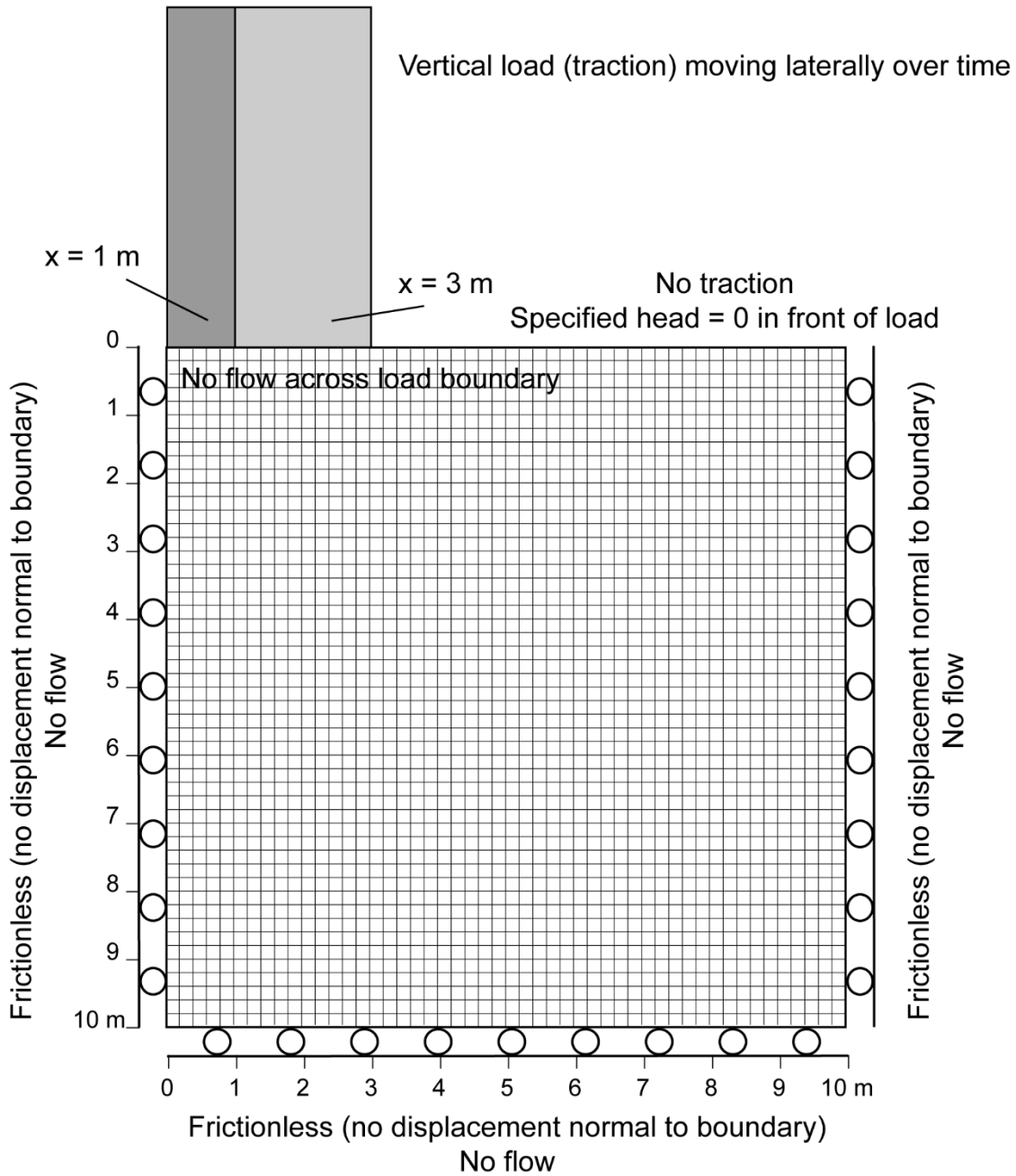


Figure S5. Finite-element domain used for Biot modeling of poroelastic response in alluvium to vertical loading on the upper surface from an overriding landslide. Domain is 10 m by 10 m with 10 cm square elements (20 cm elements shown for clarity). Boundary conditions shown for both displacement and groundwater flow. Vertical load moves laterally over time (at a rate of 10 m/s) to simulate advancing landslide front - loads at two steps (1 and 3 m) are shown.

APPENDIX S4. METHODOLOGY FOR CYCLIC SHEARING LIQUEFACTION EVALUATION

We evaluated cyclic liquefaction shearing potential via the cyclic stress approach (Seed and Idriss, 1971) as implemented in Kramer (1996) in which the cyclic stress ratio (*CSR*), as a mechanism for soil forcing, is compared to the cyclic resistance ratio (*CRR*), as a measure of soil resistance to liquefaction. The factor of safety against liquefaction is therefore defined as CRR/CSR and a value less than 1 indicates probable liquefaction. Although the method is empirical and was developed for ground shaking resulting from earthquakes, it can serve as a proxy for other vibratory motions as well (e.g., Hryciw et al., 1990; Pando et al, 2001; Ashford et al., 2006).

The *CRR* is calculated from empirical charts relating some form of soil strength to case studies where liquefaction from cyclic shaking did (and did not) occur. We used standard penetration test (SPT) data (i.e., *N* values) collected from underlying North Fork Stillaguamish River alluvium at the distal ends of the landslide deposit during reconstruction of SR 530 (Fiske, 2014) and implemented SPT correction factors according to standard methods (e.g., Coduto, 1994, see Section 4.3) to arrive at an average value of $N_{1,60} = 3$ for the uppermost layer of the alluvium (at approximate 2 m depth) (Table S6). Whereas SPT values in some other boreholes had higher *N* values, we selected the data presented in Table S6 as representative of the loosest layer that was likely capable of liquefying. The four boreholes listed in Table S6 were located along a 1.3 km-long transect across the length of the valley and thus represented a wide cross section of the alluvial floodplain overridden by the Oso landslide.

Using standard liquefaction charts for SPT data (e.g., Fig. 9.31 in Kramer, 1996) and a 15% fines content (typical for the North Fork Stillaguamish River alluvium; Fig. 14), we obtained a preliminary CRR value of 0.08 for an equivalent magnitude 7.5 earthquake. The simplified procedure requires the CRR value to be corrected for three items: the earthquake magnitude (using a Magnitude Scaling Factor, MSF), sloping ground (using a K_α value), and overburden (using a K_σ value):

$$CRR = CRR_{M,\alpha,\sigma} = CRR_{field} MSF \cdot K_\alpha K_\sigma. \quad (S1a)$$

We used current research results from Boulanger and Idriss (2015) to compute the MSF . For a M_w 5.25 earthquake (the lowest of which typical MSF correlations have been developed) and an $N_{60'}$ value of 3, the MSF is 1.10. Other MSF relations (e.g., Youd et al., 2001) indicate higher values, but these earlier relations do not account for the low strength response of very loose soils (i.e., $N_{1,60} = 3$). Further, the shape of the MSF relation for such loose soils would not likely provide a significant increase in MSF value for still lower magnitude (i.e., $< M_w$ 5.25) ground shaking, such as was likely generated from the Oso landslide. For the North Fork Stillaguamish River floodplain, no sloping ground correction is needed ($K_\alpha = 1.0$), and the overburden is thin such that K_σ is 1.1. The field equivalent liquefaction resistance CRR is therefore:

$$CRR = CRR_{M,\alpha,\sigma} = (0.08)(1.10)(1.0)(1.1) = 0.097. \quad (S1b)$$

The CSR is defined as:

$$CSR = 0.65 \frac{a_{max}}{g} \frac{\sigma_{vo}}{\sigma_{vo'}} r_d, \quad (S2a)$$

where a_{max} is the peak ground acceleration (pga), g is the gravitational constant (9.81 m/s^2), σ_{vo} and σ_{vo}' are the total and effective vertical overburden stress at the depth of interest, and r_d is a depth reduction factor.

We computed a_{max} at the site by scaling seismometer data recorded at a station 11.5 km from the Oso landslide (Pacific Northwest Seismic Network, Station JCW - <https://pnsn.org/seismogram/current/jcw> with data available from <https://service.iris.edu/irisws/timeseries/1/>). During the Oso landslide, the pga (vertical motion only) was $6.53 \times 10^{-4} \text{ m/s}^2$. To scale this data to the Oso site, we compared seismologic records collected at three USGS “spider” units (OSO1, OSO2, OSO3, data available from USGS upon request) placed at the slide in the days following the landslide as part of USGS efforts to monitor ongoing landslide motion during the rescue and recovery efforts. The spiders recorded several small mass movement events in the weeks that followed the landslide; these included a till fall on 25 April 2014 when a piece of the headscarp was observed to first slide and then fall onto the rotated block of the Whitman slide. The impacts made by this event were recorded both at the spiders and at the JCW station, thereby allowing a scaling correction factor to be computed for the pga recorded between these stations (K. Allstadt, pers. comm.). During the sliding motion of the 25 April 2014 till fall, the Oso spiders recorded pga values between 0.03 and 0.10 m/s^2 . During the falling motion, the spiders recorded pga values between 0.25 m/s^2 and 0.28 m/s^2 . At JCW, the sliding and falling motions could similarly be distinguished, with pga values of $7.37 \times 10^{-5} \text{ m/s}^2$ and $1.22 \times 10^{-4} \text{ m/s}^2$, respectively. Neglecting the sliding portion of the time series for the OSO1 spider (which appeared to have anomalous data), we calculated resultant pga ratios (Oso spider/JCW) of 1,259 for sliding and 2,174 (a minimum

value due to inadvertent clipping of the source record) for falling. Multiplying these ratios by the p_{ga} value of the JCW record during the Oso landslide results in p_{ga} (a_{max}) values of 0.822 m/s^2 using the sliding ratio and 1.42 m/s^2 using the falling ratio. As the Oso landslide was primarily a sliding motion, we used the sliding (and lower value) of a_{max} for our calculation of CSR.

We computed σ_{vo} and σ_{vo}' at 2 m depth using a total unit weight of 18.9 kN/m^3 , assuming full saturation and based on specific gravity and void ratio from undisturbed samples of river alluvium (Appendix S1, Table S2 – surface alluvium). This yielded an effective-stress ratio ($\frac{\sigma_{vo}}{\sigma_{vo}'}$) equal to 2.08. Finally, for near-surface conditions, no depth reduction factor was needed and r_d was therefore 1.0 (Seed and Idriss, 1971). Putting these components together into equation S2a resulted in:

$$CSR = 0.65 \frac{0.822}{9.81} \frac{37.8}{18.2} 1.0 = 0.113. \quad (S2b)$$

Calculating the factor of safety (F_s) against liquefaction:

$$F_s = \frac{CRR}{CSR} = 0.9, \quad (S3)$$

thereby indicates (i.e., $F_s < 1$) that liquefaction could have occurred under these ground and vibration conditions.

TABLE S6. SPT DATA OF ALLUVIUM IN THE VICINITY OF STATE ROUTE 530 (SR530)
RECONSTRUCTION

Borehole	SPT N value*	Depth (m)	Efficiency (%)	SPT N_{60} value [†]	Overburden corr. factor C_N^{\S}	SPT $N_{1,60}$ value
E-1-14	0	2.0	83.8	0	1.37	0
C-2-14	2	2.4	90.1	2	1.35	3
C-4p-14	0	1.5	83.8	0	1.40	0
C-5p-14	6	1.0	83.8	6	1.43	9
Average	N.A. [#]	N.A.	N.A.	N.A.	N.A.	3

*SPT N values are from Fiske (2014).

[†]SPT correction factors are: $C_B=1.0$ for 10-11 cm (4.0-4.5 inch) borehole, $C_S=1.0$ for standard sampler, $C_R=0.75$ for 3.3 m (10 ft) rod length.

[§] C_N correction factor calculated using Skempton (1986) based on depth and a 18.9 kN/m³ unit weight for either normally consolidated fine or coarse sand in the alluvial sediment.

[#]N.A. = not applicable.

APPENDIX REFERENCES

Amini, F. and Qi, G.Z., 2000, Liquefaction testing of stratified silty sands: *Journal of Geotechnical and Geoenvironmental Engineering*, v. 126, no. 3, p. 208-217.

Ashford, S.A., Juirnarongrit, T., Sugano, T., and Hamada, M., 2006, Soil–pile response to blast-induced lateral spreading. I: field test: *Journal of Geotechnical and Geoenvironmental Engineering*, v. 132, no. 2, p. 152-162, doi: 10.1061/(ASCE)1090-0241(2006)132:2(152).

ASTM D422-63, 2007, Standard test method for particle-size analysis of soils: West Conshohocken, Pennsylvania, ASTM International, www.astm.org.

ASTM D854-14, 2014, Standard test methods for specific gravity of soil solids by water pycnometer: West Conshohocken, Pennsylvania, ASTM International, www.astm.org.

ASTM D2216-10, 2010, Standard test methods for laboratory determination of water (moisture) content of soil and rock by mass: West Conshohocken, Pennsylvania, ASTM International, www.astm.org.

ASTM D2487-11, 2011, Standard practice for classification of soils for engineering purposes (Unified Soil Classification System): West Conshohocken, Pennsylvania, ASTM International, www.astm.org.

ASTM D4318-10e1, 2010, Standard test methods for liquid limit, plastic limit, and plasticity index of soils: West Conshohocken, Pennsylvania, ASTM International, www.astm.org.

ASTM D7263-09, 2009, Standard test methods for laboratory determination of density (unit weight) of soil specimens: West Conshohocken, Pennsylvania, ASTM International, www.astm.org.

Badger, T.C., 2016, SR 530 Landslide Geotechnical Study: Olympia, Washington, Washington State Department of Transportation Geotechnical Data Report, May 2016, 355p.

Biot, M.A., 1941, General theory of three-dimensional consolidation: *Journal of Applied Physics* v. 12, p. 155-164.

Boulanger, R.W., and Idriss, I.M., 2015, Magnitude scaling factors in liquefaction triggering procedures: *Soil Dynamics and Earthquake Engineering*, v. 79, no. B, p. 296-303, doi:10.1016/j.soildyn.2015.01.004.

Coduto, D.P., 1994, *Foundation design, principles and practices*: Englewood Cliffs, New Jersey, Prentice Hall, 796 p.

Cubrinovski, M. and Ishihara, K., 2002, Maximum and minimum void ratio characteristics of sands: *Soils and Foundation*, v. 42, no. 6, p. 65-78.

Fiske, A.J., 2014, SR 530 Skaglund Hill Vic. To C-Post Rd. Vic. Emergency Roadway Reconstruction: Washington State Department of Transportation Geotechnical Data Report (DMA-153, MP36.8-38.4), May 7, 2014, 138 p.

Hryciw, R.D., Vitton, S., and Thomann, T.G., 1990, Liquefaction and flow failure during seismic exploration: *Journal of Geotechnical Engineering*, v. 116, no. 12, p. 1881-1899, doi:10.1061/(ASCE)0733-9410(1990)116:12(1881).

- Hsieh, P.A., 1996, Deformation-induced changes in hydraulic head during ground-water withdrawal: *Ground Water*, v. 34, p. 1082-1089.
- Iverson, R.M., George, D.L., Allstadt, K., Reid, M.E., Collins, B.D., Vallance, J.W., Schilling, S.P., Godt, J.W., Cannon, C.M., Magirl, C.S., Baum, R.L., Coe, J.A., Schulz, W.H., and Bower, J.B., 2015, Landslide mobility and hazards—implications of the 2014 Oso disaster: *Earth and Planetary Science Letters*, v. 412, p. 197-208, <http://dx.doi.org/10.1016/j.epsl.2014.12.020>.
- Jefferies M. and Been K., 2015, *Soil liquefaction: a critical state approach*: Boca Raton, CRC Press, 2nd Edition, 712 p.
- JIS, 2000. Test method for minimum and maximum densities of sands. Japanese Geotechnical Society, *Soil Testing Standards*, Japanese Standards Association: JIS A 1224:2000, p. 136–138 (in Japanese, translated to English by Y. Hosono).
- Kramer, S.L., 1996, *Geotechnical earthquake engineering*: Upper Saddle River, New Jersey Prentice Hall, 653 p.
- Lade, P.V., 2016, *Triaxial testing of soils*: West Sussex, UK, Wiley, 402 p.
- Magirl, C.S., Keith, M.K., Anderson, S.W., O'Connor, J.E., Aldrich, Robert, and Mastin, M.C., 2015, Preliminary assessment of aggradation potential in the North Fork Stillaguamish River downstream of the State Route 530 landslide near Oso, Washington: U.S. Geological Survey Scientific Investigations Report 2015–5173, 20 p., <http://dx.doi.org/10.3133/sir20155173>.

- Mulilis, J.P., Arulanandan, K., Mitchell, J.K., Chan, C.K. Seed, H.B., 1977, Effects of sample preparation on sand liquefaction, Journal of the Geotechnical Engineering Division, ASCE, Vol. 103, No. 2, p. 91-108.
- Pando, M.A., Olgun, C.G., and Martin, J.R. II, 2001, Liquefaction potential of railway embankments: Missouri University of Science and Technology, International Conferences on Recent Advances in Geotechnical Earthquake Engineering and Soil Dynamics, paper no. 2.29, 6 p., <http://scholarsmine.mst.edu/icrageesd/04icrageesd/session02/16>.
- Rice, J.R. and Cleary, M.P., 1976, Some basic stress diffusion solutions for fluid-saturated elastic porous media with compressible constituents: Reviews of Geophysics, v. 14, no. 2, p. 227-241.
- Seed, H.B. and Idriss, I.M., 1971, Simplified procedure for evaluating soil liquefaction potential: Journal of the Soil Mechanics and Foundations Division (American Society of Civil Engineers), v. 97, p. 1249-1273.
- Skempton, A.W., 1986, Standard penetration test procedures and the effects in sands of overburden pressure, relative density, particle size, aging and overconsolidation: Géotechnique, v. 36, no. 3, p. 425-447.
- Terzaghi, K., Peck, R. B., and Mesri, G., 1996, Soil mechanics in engineering practice: New York, John Wiley & Sons, 549 p.
- Wood, D.M., 1991, Soil behaviour and critical state soil mechanics: Cambridge, Cambridge University Press, 488 p.

Youd, T.L. and others, 2001, Liquefaction resistance of soils: summary report from the 1996 NCEER and 1998 NCEER/NSF workshops on evaluation of liquefaction resistance of soils: Journal of Geotechnical and Geoenvironmental Engineering, v. 127, no. 10, p. 817-833, doi:10.1061/(ASCE)1090-0241(2001)127:10(817).